

# Evidence-aware Integration and Domain Identification of Spatial Transcriptomics Data

Wei Zhang<sup>1</sup>, Siyu Yi<sup>2\*</sup>, Lezhi Chen<sup>3</sup>, Yifan Wang<sup>4</sup>, Ziyue Qiao<sup>5</sup>,  
Yongdao Zhou<sup>6</sup>, Wei Ju<sup>1\*</sup>

<sup>1</sup> College of Computer Science, Sichuan University, Chengdu, China

<sup>2</sup> College of Mathematics, Sichuan University, Chengdu, China

<sup>3</sup> College of Electrical Engineering, Sichuan University, Chengdu, China

<sup>4</sup> School of Information Technology & Management, University of International Business and Economics, Beijing, China

<sup>5</sup> School of Computing and Information Technology, Great Bay University, Dongguan, China

<sup>6</sup> NITFID, School of Statistics and Data Science, Nankai University, China

wayc04@gmail.com, {siyuyi, juwei}@scu.edu.cn, chenlezhi@stu.scu.edu.cn, yifanwang@uibe.edu.cn,  
zyqiao@gbu.edu.cn, ydzhou@nankai.edu.cn

## Abstract

Spatial transcriptomics (ST) enables joint profiling of gene expression and spatial positions, thereby revealing spatially resolved biological functions. However, many existing ST analysis methods often fail to explicitly quantify the belief and uncertainty in decisions caused by noisy ST data, making it difficult to handle spots of varying quality in a fine-grained manner. In addition, domain identification is a fundamental and critical task in ST, but commonly used models that separate expression learning and clustering often struggle to learn cluster-friendly latent representations effectively. To address these issues, we propose PREST, a prototype-based evidence-aware integration framework for ST data. PREST performs multi-scale representation learning with fine-grained attention fusion and introduces learnable class prototypes to quantify belief and uncertainty in model decisions. We aim to align overall belief scores with latent semantic information to enhance uncertainty quantification and prototype learning, thereby promoting the learning of clustering-friendly representations. PREST further integrates an uncertainty-aware reconstruction module and spatial regularization to reduce overfitting to unreliable spots and promote denoised, discriminative representations. Extensive experiments on several benchmark datasets validate the effectiveness and superiority of our proposed PREST across various downstream tasks.

**Code** — <https://github.com/wayc04/PREST>

**Appendix** — <https://github.com/wayc04/PREST>

## Introduction

Spatial transcriptomics (ST) captures gene expression while preserving the spatial context of spots within tissue sections (Williams et al. 2022), enabling comprehensive analysis of tissue architecture and cellular organization (Rao et al. 2021; Asp, Bergenstråhle, and Lundeberg 2020). By jointly profiling molecular and spatial information, ST provides unprecedented insights into how cells interact and

function within their native environments. Current ST technologies can be broadly categorized into imaging-based *in situ* methods, such as MERFISH (Moffitt et al. 2018), osm-FISH (Codeluppi et al. 2018) and seqFISH (Lubeck et al. 2014; Shah et al. 2016), and barcode-based sequencing approaches, including 10x Visium (Ji et al. 2020), SLIDE-seq (Rodrigues et al. 2019), and Stereo-seq (Chen et al. 2022). Since the resolution of most platforms does not reach single-cell level, gene expression is measured at discrete units called *spots*, each aggregating transcripts from multiple cells. Despite this limitation, ST has rapidly become a cornerstone technology in spatial genomics and has motivated the development of numerous computational methods tailored to analyze such data.

ST integrates gene expression and spatial information to decode biological processes, such as cell distribution, gene regulation, and tissue heterogeneity, offering deeper insights into tissue organization and function. Early approaches primarily employed unsupervised algorithms, including PCA,  $k$ -means (Likas, Vlassis, and Verbeek 2003) and Louvain (Blondel et al. 2008). These methods treat spots as independent observations and overlook the spatial continuity inherent in tissues. To better capture spatial dependencies, recent methods have leveraged graph-based approaches, particularly *Graph Neural Networks* (GNNs, Kipf and Welling 2017; Veličković et al. 2018; Ju et al. 2024b, 2025), which represent spots as nodes in a graph and incorporate both gene expression and neighborhood relationships (Liu et al. 2023; Li et al. 2022; Dong and Zhang 2022; Zhu et al. 2024). DeepST (Xu et al. 2022) pioneers domain identification with deep learning, enabling effective batch integration. GraphST (Long et al. 2023) builds on this with self-supervised contrastive learning, improving clustering and multi-slice analysis. SpaGCN (Hu et al. 2021) then uses graph convolution to integrate gene expression and spatial data, detecting coherent expression patterns. stMMR (Zhang et al. 2024) enhances this with self-attention for robust multimodal learning, while DUSTED (Zhu et al. 2025) combines gene channel and attention in a graph autoencoder to capture spatial features and expression variability.

\*Corresponding authors

Copyright © 2026, Association for the Advancement of Artificial Intelligence (www.aaai.org). All rights reserved.

Despite the success of existing ST analysis methods, several intrinsic limitations remain. (1) *First*, ST data is inherently noisy due to low capture efficiency and shallow sequencing depth stemming from cost control or technical constraints, as well as biological factors such as variations in cell permeability that cause mRNA drift or diffusion (Du et al. 2024). These factors lead to high sparsity and over-dispersion in ST data, introducing uncertainty in downstream analyses and decisions. Existing methods often denoise data implicitly without explicitly modeling the belief and uncertainty of model decisions, including autoencoder-based (Xu et al. 2022; Long et al. 2023; Zhu et al. 2025), smoothing-based (Holdener and De Vlaminck 2025), and image-enhanced approaches (Wang et al. 2022). These methods typically treat noise as an undesirable factor to be removed, processing all spots equally without indicating which ones are unreliable, and may overfit to low-quality or boundary regions. (2) *Second*, clustering analysis serves as the foundation for many ST downstream tasks, including spatial domain identification, cell type annotation, differentially expressed gene detection, and trajectory inference. However, many deep learning-based ST methods focus primarily on representation learning while neglecting the modeling of class information. A common paradigm involves first learning embeddings and then performing clustering on them using algorithms such as  $k$ -means, Leiden, Louvain, or GMM (Long et al. 2023; Zhang et al. 2024; Zhu et al. 2025). This two-step process is often not clustering-friendly, resulting in suboptimal performance in downstream analyses.

To address these issues, we propose the Prototype-based Evidence-aware Integration Framework for Spatial Transcriptomics data (PREST). We begin by performing multi-scale representation learning followed by fine-grained cross-attention fusion. Then, we introduce learnable class prototypes to capture cluster information and utilize subjective logic (SL, Jøsang 2016) to explicitly quantify both *evidence / belief* and *uncertainty* of model decisions caused by noisy or dropout ST data. To enhance the reliability of these quantifications and prototype learning, we impose constraint to encourage the belief scores to capture the overall semantic information in the latent space. To effectively handle the highly sparse nature of ST data, we adopt the zero-inflated negative binomial (ZINB, Yu et al. 2022) model to reconstruct original expressions. We also leverage spatial coordinates to regularize spot representations, enabling learning discriminative representations enriched with spatial context. Furthermore, we incorporate quantified uncertainties into reconstruction and regularization to assess spot reliability, enabling the model to softly down-weight low-belief regions. It reduces overfitting to low-quality data and enhances overall model trustworthiness. Finally, we conduct various downstream analyses based on the learned spot representations and class prototypes. Extensive experiments on multiple datasets show the superiority of our framework.

## Preliminaries & Problem Definition

**Notations.** Let  $\mathbf{P} = \{(u_i, v_i)\}_{i=1}^N$  denote the spatial coordinates of  $N$  spots and  $\mathbf{X} = (\mathbf{x}_1, \dots, \mathbf{x}_N)^\top \in \mathbb{R}^{N \times G}$  be the

gene expression matrix after preprocessing, where  $G$  is the number of genes and  $\mathbf{x}_i \in \mathbb{R}^G$  corresponds to the expression profile at spot  $i$ . The objective is to learn class prototypes  $\mathbf{T} = (t_1, \dots, t_K)^\top \in \mathbb{R}^{K \times D}$  and spot representations  $\mathbf{Z} = (z_1, \dots, z_N)^\top \in \mathbb{R}^{N \times D}$  with  $D \ll G$  that jointly encodes both the spatial positions and gene expressions.

**Downstream Analyses.** We perform several downstream analysis tasks, including: (i) *Domain identification (or spatial clustering)*, which assigns coherent regions by grouping similar representations; (ii) *Differentially expressed gene (DEG) detection*, which identifies marker genes characteristic of each spatial domain; (iii) *Expression imputation*, which predicts missing or unobserved gene expression values to enhance data completeness and downstream analysis. and (iv) *Enrichment analysis*, which interprets the biological significance of identified genes or clusters by linking them to known pathways or ontologies.

## Methodology

In this section, we introduce a novel framework, PREST, designed for domain identification and related downstream analyses in ST. The framework is composed of three key modules: (i) *Multi-scale Representation Extraction and Fusion*; (ii) *Prototype-based Belief and Uncertainty Estimation*; and (iii) *Uncertainty-weighted Expression Reconstruction and Spatial Regularization*. An overview of the entire pipeline is depicted in Figure 1.

### Multi-scale Representation Extraction and Fusion

ST enables the identification of similar cells by incorporating spatial context. To effectively utilize this spatial information and take advantage of the expressive power of GNNs, we first transform the spatial coordinates  $\mathbf{P}$  into an undirected graph. Specifically, we construct the spatial adjacency matrix  $\mathbf{A}$  using a fixed-radius nearest neighbor approach, and assign the expression matrix  $\mathbf{X}$  as the node attributes.

In GNNs, the graph convolutional network (GCN, Kipf and Welling 2017) updates node representations by aggregating information from their neighbors, thereby effectively capturing the structural patterns of graph data. The layer-wise propagation rule of a GCN is typically defined as:

$$\mathbf{Z}^{s,(l+1)} = \sigma(\tilde{\mathbf{A}}\mathbf{Z}^{s,(l)}\mathbf{W}^{s,(l)}), \quad (1)$$

where  $\tilde{\mathbf{A}}$  denotes the normalized adjacency matrix,  $\mathbf{W}^{s,(l)}$  is the trainable weight matrix, and  $\sigma(\cdot)$  is a non-linear activation function. In contrast, multi-layer perceptrons (MLPs) operate purely on node attributes, making them particularly effective at capturing semantic patterns embedded in attribute space. A standard MLP layer can be form

$$\mathbf{Z}^{e,(l+1)} = \phi\left(\mathbf{Z}^{e,(l)}\mathbf{W}^{e,(l)} + \mathbf{b}^{e,(l)}\right), \quad (2)$$

where  $\mathbf{W}^{e,(l)}$  and  $\mathbf{b}^{e,(l)}$  are learnable parameters, and  $\phi(\cdot)$  is an activation function such as ReLU. To further enhance representational capacity and stabilize training, each encoder layer can be augmented with self-attention (Vaswani et al. 2017) and skip connection (He et al. 2016), which help mitigate issues like vanishing or exploding gradients.

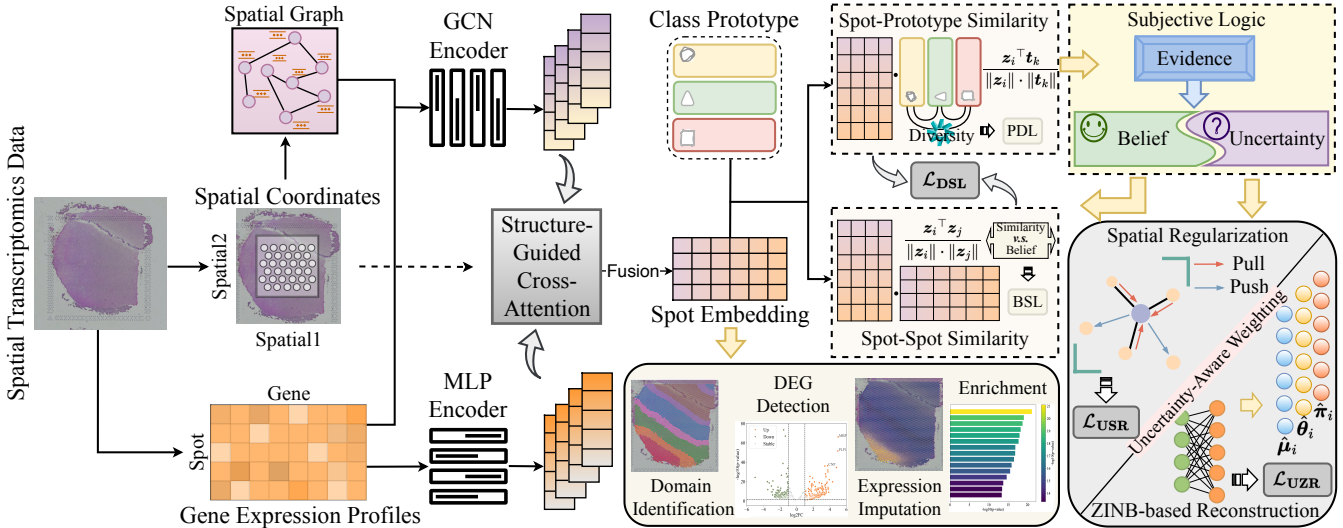


Figure 1: Illustration of the proposed framework PREST.

In ST data, due to technical limitation or biological variation, the measured expression data can be inherently noisy. Meanwhile, due to limitations in imaging resolution, tissue deformation, or inaccuracy in graph construction heuristics, the spatial graph may be also not precise. In such cases, when expression signals are strong but the spatial structure is unreliable, MLPs can help mitigate the influence of noisy connections by focusing on attribute-driven features. Conversely, when expression is sparse or noisy, the spatial topology can provide useful contextual cues that GCN is well-suited to exploit. Even in challenging scenarios where both gene expression and spatial structure are affected by noise, learning from multiple scales remains beneficial, as it enables the model to integrate complementary patterns across views and attenuate view-specific noise. To this end, we integrate GCN and MLP into a unified framework for multi-scale representation learning, facilitating the extraction of more robust and informative embeddings.

Based on the embeddings obtained from GCN and MLP encoders, denoted as  $\mathbf{Z}^s$  and  $\mathbf{Z}^e$ , we introduce a structure-guided cross-attention mechanism (CroAtt) to perform fine-grained representation fusion. The fusion process is:

$$\mathbf{Z} = \text{Norm} \left( \text{CroAtt}(\mathbf{Z}^s, \mathbf{Z}^e) + \text{CroAtt}(\mathbf{Z}^e, \mathbf{Z}^s) \right), \quad (3)$$

$$\text{CroAtt}(\mathbf{Z}^s, \mathbf{Z}^e) = \text{Softmax} \left( \text{Mask} \left( \frac{\mathbf{Z}^e \mathbf{Z}^{s\top}}{\sqrt{D}}, \mathbf{A} \right) \right) \mathbf{Z}^s.$$

This mechanism dynamically evaluates the contribution of spatial- and expression-level representations to one another, thereby enabling adaptive and content-aware fusion. The masking operation based on the spatial adjacency matrix helps eliminate redundant or spurious dependencies, ensuring that the attention is focused on meaningful local interactions. By explicitly modeling fine-grained dependencies across the two encoder outputs, rather than performing naive cross-view averaging, it facilitates a more comprehensive integration of spatial and expression information.

## Prototype-based Belief and Uncertainty Estimation

The presence of inherent noise in the ST data inevitably leads to predictive uncertainty (Malinin and Gales 2018). Therefore, while ensuring representation richness through multi-scale extraction, it is also crucial to quantify the decision uncertainty of the fused information and leverage it to enhance model training. To this end, we adopt subjective logic (SL, Jøsang 2016; Li et al. 2023) to characterize the *belief* or *evidence* of domain identification decision, as well as the *uncertainty* caused by the lack of sufficient evidence.

Formally, a spot  $i$  ( $i \in \{1, \dots, N\}$ ) in SL is associated with a multinomial opinion consisting of a belief mass distribution  $\{b_{ik}\}_{k=1}^K$  over  $K$  clusters and an uncertainty value  $u_i$ , satisfying the constraint  $\sum_{k=1}^K b_{ik} + u_i = 1$  and  $b_{ik}, u_i \geq 0$ . Let  $e_{ik} ( \geq 0 )$  represent the extracted evidence from data supporting the association of spot  $i$  with cluster  $k$ . The belief and uncertainty are then computed as:

$$b_{ik} = \frac{e_{ik}}{\sum_{k=1}^K (e_{ik} + 1)}, \quad u_i = \frac{K}{\sum_{k=1}^K (e_{ik} + 1)}. \quad (4)$$

To facilitate the learning of cluster-relevant evidence and support domain identification, we introduce learnable class prototypes  $\mathbf{T} = (t_1, \dots, t_K)^\top$ , initialized via k-means on pre-trained spot embeddings (details provided in the Experiment Section). Based on this and fused representation matrix  $\mathbf{Z} = (z_1, \dots, z_N)^\top$  from Eq. (3), we define the spot-to-prototype similarity matrix  $\mathbf{E} = (E_{ik}) \in \mathbb{R}^{N \times K}$  and the spot-to-spot similarity matrix  $\mathbf{S} = (S_{ij}) \in \mathbb{R}^{N \times N}$  as:

$$E_{ik} = \frac{z_i^\top t_k}{\|z_i\| \cdot \|t_k\|}, \quad S_{ij} = \frac{z_i^\top z_j}{\|z_i\| \cdot \|z_j\|}. \quad (5)$$

The similarity score  $E_{ik}$ , after applying a positive activation, can be interpreted as the evidence  $e_{ik}$ , allowing us to compute belief score  $b_{ik}$  and uncertainty  $u_i$  according to Eq. (4).

To ensure meaningful quantification, we first impose constraints on the class prototypes by encouraging high diversity among them, which promotes better separability. To this

end, we introduce a prototype diversity learning (PDL) loss:

$$\mathcal{L}_{\text{PDL}} = \frac{1}{2K(K-1)} \sum_{1 \leq k < k' \leq K} \left( \frac{\mathbf{t}_k^\top \mathbf{t}_{k'}}{\|\mathbf{t}_k\| \cdot \|\mathbf{t}_{k'}\|} \right)^2.$$

With the prototypes, to ensure better uncertainty quantification, the prototype-based beliefs should effectively encapsulate the global semantic structure of the data in the latent space. To encourage this, we require that the total beliefs assigned to a spot aligns closely with its total similarities to all other spots. Accordingly, we introduce the belief-based semantics learning (BSL) loss:

$$\mathcal{L}_{\text{BSL}} = \frac{1}{N} \sum_{i=1}^N \left( \frac{1}{K} \sum_{k=1}^K b_{ik} - \frac{\lambda}{N} \sum_{j=1, j \neq i}^N S_{ij} \right)^2,$$

where  $\lambda$  is a scaling factor that compensates for potential differences in magnitude. We then formulate a joint diversity-semantics learning loss (DSL) as:

$$\mathcal{L}_{\text{DSL}} = \mathcal{L}_{\text{PDL}} + \mathcal{L}_{\text{BSL}}. \quad (6)$$

### Uncertainty-weighted Expression Reconstruction and Spatial Regularization

To effectively handle highly sparse ST data and impute dropout values, we introduce a ZINB-based decoder built upon the fused representations to reconstruct the original gene expression in a self-supervised manner. It is worth noting that the raw expression data may contain noise; thus, different spots should be assigned different self-supervision weights to prevent overfitting on low-quality data. Technically, we leverage the uncertainty estimated in Eq. (4) to reweight the loss, assigning lower weights to spots with higher uncertainties. It leads to the uncertainty-weighted ZINB-based reconstruction (UZR) loss:

$$\mathcal{L}_{\text{UZR}} = - \sum_{i=1}^N \omega_i \log \text{ZINB}(\mathbf{x}_i | \hat{\boldsymbol{\mu}}_i, \hat{\boldsymbol{\theta}}_i, \hat{\boldsymbol{\pi}}_i), \quad (7)$$

$$\text{with } \omega_i = \frac{1/u_i}{\sum_{j=1}^N 1/u_j},$$

where  $\hat{\boldsymbol{\mu}}$ ,  $\hat{\boldsymbol{\theta}}$ , and  $\hat{\boldsymbol{\pi}}$  denote the estimations of ZINB parameters  $\boldsymbol{\mu}$  (the expected gene expression),  $\boldsymbol{\theta}$  (the over-dispersion characteristic of count-based data), and  $\boldsymbol{\pi}$  (the dropout probability arising from technical noise or low expression levels). With the dropout indicator function  $\delta_0(\cdot)$ , the ZINB distribution is formulated as:

$$\text{ZINB}(\mathbf{x} | \boldsymbol{\mu}, \boldsymbol{\theta}, \boldsymbol{\pi}) = \boldsymbol{\pi} \delta_0(\mathbf{x}) + (1 - \boldsymbol{\pi}) \text{NB}(\mathbf{x}), \text{ with}$$

$$\text{NB}(\mathbf{x} | \boldsymbol{\mu}, \boldsymbol{\theta}) = \Gamma(\mathbf{x} + \boldsymbol{\theta}) [\boldsymbol{\theta} / (\boldsymbol{\theta} + \boldsymbol{\mu})]^\boldsymbol{\theta} [\boldsymbol{\mu} / (\boldsymbol{\theta} + \boldsymbol{\mu})]^\mathbf{x} / [\mathbf{x}! \Gamma(\boldsymbol{\theta})].$$

We utilize three distinct MLPs ( $g_{\text{enc}}$ ) to estimate the parameters of the ZINB distribution from the fused latent representation  $\mathbf{z}_i$ . Specifically, each MLP is responsible for predicting one of the distribution parameters:

$$\hat{\boldsymbol{\mu}}_i = \text{Exp}(g_{\text{dec1}}(\mathbf{z}_i)), \hat{\boldsymbol{\theta}}_i = \text{Softplus}(g_{\text{dec2}}(\mathbf{z}_i)),$$

$$\hat{\boldsymbol{\pi}}_i = \text{Sigmoid}(g_{\text{dec3}}(\mathbf{z}_i)), i \in \{1, \dots, N\},$$

where the use of non-linear activations ensures the validity of the parameter ranges required by the ZINB distribution.

To preserve the intrinsic spatial structure in the latent space and also enhance the discriminative power of learned representations, we introduce a spatial regularization loss that encourages neighboring spots to have similar representations while pushing apart those that are not spatially connected. Specifically, with  $\mathbf{A} = (A_{ij})$ , we define the uncertainty-weighted spatial regularization (USR) loss as:

$$\mathcal{L}_{\text{USR}} = - \sum_{i=1}^N \omega_i \left[ \sum_{A_{ij}=1} \log \phi(S_{ij}) + \sum_{A_{iq}=0} \log(1 - \phi(S_{iq})) \right], \quad (8)$$

where  $S_{ij}$  is defined in Eq. (5) and  $\phi(\cdot)$  is a sigmoid function that transforms the similarity scores into the range  $[0, 1]$ . The weight  $\omega_i$ , consistent with the definition in Eq. (8), is similarly designed to down-weight the supervisory signals from spurious structures on the latent representations, thereby enabling the model to learn spot representations that better reflect the underlying patterns of the ST data.

**Joint Optimization.** In summary, the proposed PREST framework combines three loss components: (i) the joint diversity-semantics learning loss  $\mathcal{L}_{\text{DSL}}$ , (ii) the ZINB-based reconstruction loss  $\mathcal{L}_{\text{UZR}}$ , and (iii) the spatial regularization loss  $\mathcal{L}_{\text{USR}}$ . The overall training objective is formulated as:

$$\mathcal{L} = \mathcal{L}_{\text{DSL}} + \alpha \mathcal{L}_{\text{UZR}} + \beta \mathcal{L}_{\text{USR}}, \quad (9)$$

where  $\alpha$  and  $\beta$  are tunable coefficients that balance the influence of reconstruction and spatial constraints.

After training converges, domain identification is achieved by aligning the optimized spot representations with the class prototypes through belief-based matching. Then the clustering results are used for various downstream analyses to validate the domain identification outcomes. The training procedure of our proposed PREST is summarized in Algorithm 1 in the Appendix.

## Experiments

### Experimental Setup

To validate the superiority of our proposed PREST, we conduct extensive experiments on three benchmark *datasets*, i.e., DLPFC (Maynard et al. 2021), HBC (Buache et al. 2011), and MAB (Dong 2008). We conduct comparisons on the performance of domain identification with several state-of-the-art *models*, including SCANPY (Wolf, Angerer, and Theis 2018), SpaGCN (Hu et al. 2021), STAGATE (Dong and Zhang 2022), DeepST (Xu et al. 2022), stLearn (Pham et al. 2023), SCGDL (Liu et al. 2023), GraphST (Long et al. 2023), stMMR (Zhang et al. 2024), and DUSTED (Zhu et al. 2025). We adopt *supervised* metrics, i.e., ARI (Vinh, Epps, and Bailey 2009), NMI (Pfitzner, Leibbrandt, and Powers 2009) and Jaccard similarity coefficient (Levandowsky and Winter 1971), and *unsupervised* metrics, i.e., Moran's I score (Moran 1950) to evaluate the performance of domain identification. Several downstream analyses are also performed to validate the effectiveness of PREST. Further experimental configurations and implementation details are provided in the Appendix.

Slice	Metric	SCANPY GB18	SpaGCN NM21	STAGATE NC22	DeepST NAR22	stLearn NC23	SCGDL BIB23	GraphST NC23	stMMR GS24	DUSTED AAAI25	PREST (Ours)
<b>151507</b>	ARI	0.20	0.39	0.54	0.46	0.49	0.49	0.48	<u>0.58</u>	0.46	<b>0.75</b>
	NMI	0.21	0.49	0.66	0.64	0.64	0.55	0.64	<u>0.72</u>	0.65	<b>0.78</b>
<b>151508</b>	ARI	0.15	0.33	0.49	0.46	0.31	0.34	0.49	<u>0.52</u>	0.45	<b>0.56</b>
	NMI	0.21	0.43	0.63	0.61	0.53	0.44	0.54	<u>0.64</u>	0.64	<b>0.66</b>
<b>151509</b>	ARI	0.19	0.35	0.53	0.48	0.45	0.32	0.52	<u>0.58</u>	0.45	<b>0.59</b>
	NMI	0.27	0.51	0.66	0.62	0.62	0.48	0.64	<u>0.67</u>	0.64	<b>0.69</b>
<b>151669</b>	ARI	0.10	0.23	0.35	0.42	0.32	0.24	<u>0.48</u>	0.47	0.47	<b>0.66</b>
	NMI	0.16	0.36	0.58	0.53	0.49	0.38	<u>0.59</u>	0.55	<u>0.59</u>	<b>0.64</b>
<b>151670</b>	ARI	0.09	0.33	0.32	0.36	0.23	0.26	0.46	<u>0.49</u>	0.29	<b>0.57</b>
	NMI	0.16	0.43	0.53	0.54	0.41	0.38	<u>0.68</u>	0.56	0.51	<u>0.60</u>
<b>151671</b>	ARI	0.12	0.42	0.51	0.48	0.39	0.31	0.61	<u>0.67</u>	0.50	<b>0.81</b>
	NMI	0.24	0.53	0.65	0.63	0.54	0.41	0.72	<u>0.71</u>	0.65	<b>0.79</b>
<b>151672</b>	ARI	0.12	0.52	0.54	0.44	<u>0.63</u>	0.34	0.34	0.60	0.57	<b>0.78</b>
	NMI	0.23	0.60	0.66	0.59	0.61	0.47	0.46	<u>0.71</u>	0.67	<b>0.82</b>
<b>151673</b>	ARI	0.20	0.40	0.45	0.57	0.30	0.34	<u>0.63</u>	0.60	0.57	0.59
	NMI	0.29	0.55	0.63	<u>0.71</u>	0.49	0.42	<u>0.74</u>	0.68	0.70	0.68
<b>151674</b>	ARI	0.22	0.31	0.48	0.48	0.38	0.27	0.43	<u>0.51</u>	0.46	<b>0.56</b>
	NMI	0.31	0.46	0.58	0.60	0.54	0.38	0.61	<u>0.63</u>	<u>0.63</u>	<b>0.69</b>
<b>151675</b>	ARI	0.23	0.27	0.36	0.52	0.38	0.30	0.55	<u>0.56</u>	0.56	<b>0.58</b>
	NMI	0.32	0.41	0.50	0.65	0.56	0.41	0.62	<u>0.66</u>	0.65	<b>0.68</b>
<b>151676</b>	ARI	0.22	0.31	0.49	0.50	0.40	0.29	<u>0.61</u>	0.54	0.52	<u>0.56</u>
	NMI	0.31	0.48	0.63	0.60	0.56	0.42	0.66	0.65	<u>0.67</u>	<b>0.69</b>

Table 1: Domain identification performance of different methods on the 11 slices of the DLPFC dataset. The **bold** and underlined values indicate the best and the runner-up results, respectively.

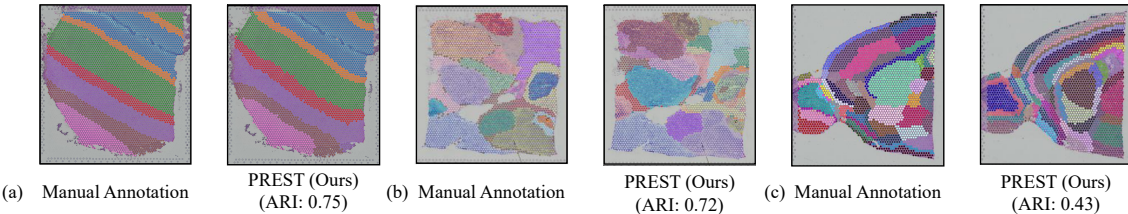


Figure 2: Spatial visualization of identification results for the DLPFC (151507), HBC, and MAB datasets.

## Experimental Results

**Quantitative Analysis.** To evaluate the domain identification performance of our PREST, we conduct quantitative comparisons with several competitive baselines on the DLPFC dataset, as summarized in Table 1. From the results, we observe that spatially-aware methods consistently outperform non-spatial counterparts, highlighting the importance of incorporating spatial context in domain identification. Notably, PREST achieves superior performance on most tissue slices, demonstrating its effectiveness and stability. We attribute this to PREST’s capability to effectively integrate spatial information while leveraging uncertainty to dynamically guide and supervise different spots, thereby preventing overfitting to low-quality data. The box plot of the results across all slices of the DLPFC dataset for various methods can be found in Figure 8 of the Appendix. Additional experimental results on HBC and MAB datasets are presented in Table 5 and the comparisons of Moran’s I score and Jaccard similarity coefficient across these datasets are shown in Table 6 of the Appendix, which further demonstrate the superiority of our proposed PREST.

**Visualization.** We visualize the domain identification results of our PREST alongside manually annotated tissues across all three datasets, with slice 151507 from the DLPFC dataset used as an example. As shown in Figure 2, our PREST performs exceptionally well in identifying spatial domains. By comparing the manual annotations with the results detected by PREST, it is clear that our method can accurately delineate spatial domains and effectively capture the boundaries between distinct tissue layers. Furthermore, for a more comprehensive comparison, including domain identification and UMAP projections of other methods, the results are displayed in Figure 7 of the Appendix, which further supports the superiority of our PREST in domain identification.

## Ablation Study and Sensitivity Analysis

**Effectiveness of Loss Function.** We conduct an ablation study to verify the effectiveness of each module we proposed, and the results are presented in Table 2. The term “PREST w/o  $\mathcal{L}_{DSL}$ ” denotes the model that excludes the  $\mathcal{L}_{DSL}$  loss, while other variants follow similar naming conventions. From the results, we observe that removing any module leads to a decrease in performance. For slice 151507

Model	Metric	DLPFC (151507)	HBC	MAB
PREST w/o $\mathcal{L}_{DSL}$	ARI	0.62	0.63	0.37
	NMI	0.70	0.67	0.63
PREST w/o $\mathcal{L}_{UZR}$	ARI	0.62	0.68	0.40
	NMI	0.72	0.69	0.69
PREST w/o $\mathcal{L}_{USR}$	ARI	0.60	0.66	0.40
	NMI	0.69	0.68	0.66
PREST (Ours)	ARI	<b>0.75</b>	<b>0.72</b>	<b>0.43</b>
	NMI	<b>0.78</b>	<b>0.73</b>	<b>0.72</b>

Table 2: Ablation study across all three datasets.

Dataset	Metric	M <sub>1</sub>	M <sub>2</sub>	M <sub>3</sub>	M <sub>4</sub>	Ours
DLPFC (151507)	ARI	0.61	0.63	0.72	0.54	<b>0.75</b>
	NMI	0.71	0.73	0.74	0.69	<b>0.78</b>
HBC	ARI	0.60	0.63	0.66	0.61	<b>0.72</b>
	NMI	0.67	0.70	0.71	0.66	<b>0.73</b>
MAB	ARI	0.32	0.30	0.35	0.30	<b>0.43</b>
	NMI	0.64	0.63	0.66	0.59	<b>0.72</b>

Table 3: Impact of different representation fusion strategies.

of the DLPFC, removing either  $\mathcal{L}_{DSL}$  or  $\mathcal{L}_{USR}$  has a considerable impact, while for HBC and MAB, removing  $\mathcal{L}_{DSL}$  shows a more significant effect. It indicates that uncertainty modeling plays a crucial role in our model.

**Influence of Representation Fusion Mechanism.** To investigate the impact of different representation fusion strategies, we compare four variants: M<sub>1</sub>: Additive fusion; M<sub>2</sub>: Learnable parameter fusion; M<sub>3</sub>: Attention score weighting; M<sub>4</sub>: Cross-attention without adjacency information. As shown in Table 3, we observe that M<sub>4</sub> performs worse than the other fusion strategies. This may be because the target spot attends to all other spots indiscriminately, which can easily introduce noise and lead to semantic ambiguity. In contrast, our structure-guided cross-attention fusion effectively leverages spatial topology by attending only to relevant neighboring spots, achieving state-of-the-art performance and underscoring the critical importance of spatial information.

**Sensitivity Analysis.** We assess hyperparameter sensitivity for  $\alpha$  and  $\beta$  in Eq. (9) across all datasets, and full results in Figure 9 (Appendix) consistently confirm model robustness.

### Uncertainty and Noise Resistance Analysis

We further investigate the role of estimated uncertainty in our PREST and the model’s robustness against noise.

**Influence of Uncertainty.** To assess the impact of evidence-aware uncertainty, we conduct an analysis on slice 151507 of DLPFC, comparing domain identification results without and with uncertainty weighting in Eqs. (7)-(8). As shown in Figure 3b, the uncertainty-weighted model (right) yields results more consistent with the ground-truth annotations (Figure 3a); for example, White Matter(WM) (pink), Layer 2 (orange), and Layer 4 (red) more closely match the true region shapes. The UMAP plots in Figure 3d further show that our model (right) learns more coherent representations for spatially distant but categorically identical spots (e.g., Layer

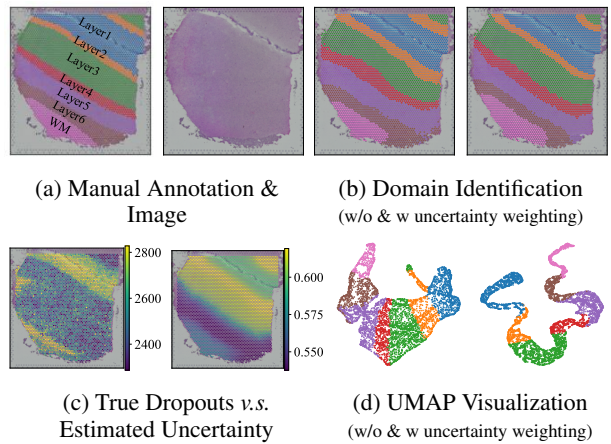


Figure 3: Visual comparison without (w/o) v.s. with (w) uncertainty weighting on slice 151507 of DLPFC.

Method	Raw	Gaussian Noise		Dropout	
		$\epsilon = 1$	$\epsilon = 5$	$p = 0.3$	$p = 0.6$
GraphST	0.41	0.21	0.15	0.32	0.15
DUSTED	0.40	0.16	0.13	0.30	0.14
PREST (Ours)	<b>0.43</b>	<b>0.30</b>	<b>0.24</b>	<b>0.36</b>	<b>0.26</b>

Table 4: Performance comparison of domain identification on MAB via ARI under different expression noise ( $\epsilon$ : variance of Gaussian noise;  $p$ : dropout probability).

2 and Layer 3), while the non-weighted version fails to do so (as seen in the left subplot of Figure 3d, where the green and orange regions are dispersed). It demonstrates that our uncertainty weighting scheme enhances the model’s ability to capture the underlying cluster structure.

**Uncertainty Attribution.** To understand the effectiveness of uncertainty weighting, we analyze the sources of uncertainty. As shown in Figure 3c (right), high-uncertainty spots are mainly located in Layers 1-3 and WM. The left panel in Figure 3c shows dropout counts per spot, with high-dropout regions concentrated in Layer 1 and WM. These observations suggest: (i) high uncertainty in Layer 1 and WM may arise from high dropout rates; while (ii) that in Layers 2-3 may result from discontinuous spatial distributions; the strong influence of spatial information on slice 151507 (see Table 2) contributes higher uncertainty in Layers 2-3. Therefore, for spots in these regions, using raw data for self-supervised learning risks overfitting; down-weighting their supervision promotes more discriminative representations.

**Robustness Analysis against Noise.** To illustrate model robustness, we artificially add various types of noise to the original dataset and compare our proposed PREST with competitive baselines. We consider Gaussian noise  $\mathcal{N}(0, \epsilon)$  (simulate inaccurate measure) with  $\epsilon = 1, 5$  and random masking (simulate dropout events) with probability  $p = 0.3, 0.6$ . Table 4 reports the results on the MAB dataset under these noise conditions. It shows that our PREST consistently outperforms GraphST and DUSTED across different

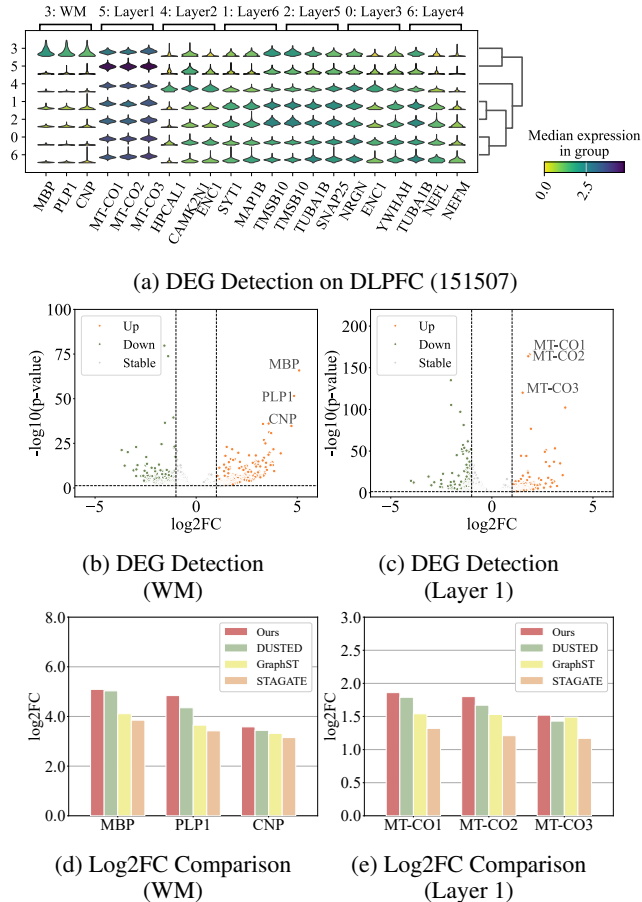


Figure 4: DEG detection on slice 151507 of DLPFC.

Gaussian noise levels and dropout rates, highlighting its superior ability to mitigate noise effects. This robustness likely stems from our uncertainty estimation mechanism, which dynamically adjusts supervision strength for each spot, preventing overfitting to low-quality data and effectively compensating for missing data patterns typical in spatial transcriptomics. Additional results on other datasets are provided in Table 7 of the Appendix.

### Downstream Analysis

We conduct differentially expressed genes (DEGs) detection, gene expression imputation, and pathway enrichment analysis (in Figure 12 of the Appendix) to highlighting the superior biological interpretability of our PREST.

**DEG Analysis.** DEGs or marker genes show statistically significant expression differences across biological conditions and serve as key indicators of tissue structure and regulation. Based on the identified domains, we perform DEG detection on all three datasets. Figure 4a presents the top three DEGs for each cluster in slice 151507 of DLPFC. For example, MBP, a gene linked to myelin formation and oligodendrocyte differentiation, is highly expressed in the WM layer, aligning with prior knowledge that oligodendro-

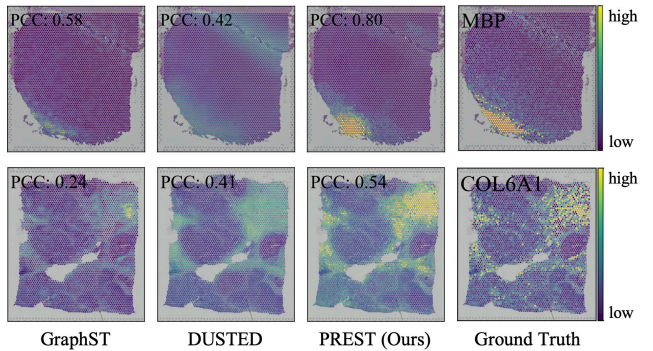


Figure 5: Visual comparison of expression imputation (MBP and COL6A1) for DLPFC and HBC, respectively.

cytes are enriched in WM (Emery 2010), thus validating our PREST biologically. We further quantify DEGs in WM and Layer 1 using volcano plots (Figures 4b-4c), showing low p-values and high log2FC values, indicating significant expression differences. Additionally, log2FC comparisons are also conducted across methods (Figures 4d-4e), which reveal that our PREST consistently achieves higher log2FC in both clusters than SCANPY, GraphST, and DUSTED, suggesting better inter-cluster separation. The detection results for other datasets are shown in Figure 10 of the Appendix.

**Gene Expression Imputation.** Due to the low capture efficiency, ST data is often significantly sparse and noisy, which poses challenges for downstream analysis. The goal of imputation is to recover the biological signal by imputing the dropouts. To validate the biologically meaningful imputation of PREST, we introduce artificial dropouts by randomly masking gene expression with a dropout rate of 0.3, and then perform reconstruction based on the remaining data. Imputation accuracy is quantified via Pearson correlation coefficient (PCC) between imputed and ground-truth expression. As demonstrated in Figure 5, our PREST achieves superior performance in both gene expression restoration and spatial pattern preservation compared to baselines (e.g., +0.22 PCC for MBP gene imputation). The results for other datasets and marker genes can be found in Figure 11 in the Appendix.

### Conclusion

In this study, we propose a prototype-based evidence-aware framework PREST for spatial transcriptomics analysis. By integrating multi-scale representation learning, structure-guided cross-attention fusion, and uncertainty-aware modules, PREST facilitates robust uncertainty estimation and clustering-friendly latent representations. Extensive experiments across multiple benchmark datasets demonstrate that our proposed PREST consistently outperforms existing approaches in accuracy of domain identification. Additional experimental analysis illustrates the interpretability of uncertainty estimation and the robustness of our PREST against noise. Various downstream analyses further reveal the effectiveness of our PREST in biological discovery.

## Acknowledgments

This work is supported in part by the National Natural Science Foundation of China under Grant 62306014, 12501344 and 12131001, Postdoctoral Fellowship Program (Grade A) of CPSF under Grant BX20250376 and BX20240239, China Postdoctoral Science Foundation under Grant 2024M762201, Sichuan Science and Technology Program under Grant 2025ZNSFSC1506 and 2025ZNSFSC0808, Sichuan University Interdisciplinary Innovation Fund, the Fundamental Research Funds for the Central Universities, LPMC, KLMDASR, and the top-notched student program of Sichuan University.

## References

Asp, M.; Bergenstråhlé, J.; and Lundeberg, J. 2020. Spatially resolved transcriptomes—next generation tools for tissue exploration. *BioEssays*, 42(10): 1900221.

Blondel, V. D.; Guillaume, J.-L.; Lambiotte, R.; and Lefebvre, E. 2008. Fast unfolding of communities in large networks. *Journal of Statistical Mechanics: Theory and Experiment*, 2008(10): P10008.

Buache, E.; Etique, N.; Alpy, F.; Stoll, I.; Muckensturm, M.; Reina-San-Martin, B.; Chenard, M.; Tomasetto, C.; and Rio, M. 2011. Deficiency in trefoil factor 1 (TFF1) increases tumorigenicity of human breast cancer cells and mammary tumor development in TFF1-knockout mice. *Oncogene*, 30(29): 3261–3273.

Chen, A.; Liao, S.; Cheng, M.; Ma, K.; Wu, L.; Lai, Y.; Qiu, X.; Yang, J.; Xu, J.; Hao, S.; et al. 2022. Spatiotemporal transcriptomic atlas of mouse organogenesis using DNA nanoball-patterned arrays. *Cell*, 185(10): 1777–1792.

Codeluppi, S.; Borm, L. E.; Zeisel, A.; La Manno, G.; van Lunteren, J. A.; Svensson, C. I.; and Linnarsson, S. 2018. Spatial organization of the somatosensory cortex revealed by osmFISH. *Nature Methods*, 15(11): 932–935.

Dong, H. W. 2008. *The Allen reference atlas: A digital color brain atlas of the C57Bl/6J male mouse*. John Wiley & Sons Inc.

Dong, K.; and Zhang, S. 2022. Deciphering spatial domains from spatially resolved transcriptomics with an adaptive graph attention auto-encoder. *Nature Communications*, 13(1): 1739.

Du, L.; Kang, J.; Hou, Y.; Sun, H.-X.; and Zhang, B. 2024. SpotGF: Denoising spatially resolved transcriptomics data using an optimal transport-based gene filtering algorithm. *Cell Systems*, 15(10): 969–981.

Emery, B. 2010. Regulation of oligodendrocyte differentiation and myelination. *Science*, 330(6005): 779–782.

Gong, C.; Zou, J.; Zhang, M.; Zhang, J.; Xu, S.; Zhu, S.; Yang, M.; Li, D.; Wang, Y.; Shi, J.; et al. 2019. Upregulation of MGP by HOXC8 promotes the proliferation, migration, and EMT processes of triple-negative breast cancer. *Molecular Carcinogenesis*, 58(10): 1863–1875.

He, K.; Zhang, X.; Ren, S.; and Sun, J. 2016. Deep residual learning for image recognition. In *Proceedings of the IEEE Conference on Computer Vision and Pattern Recognition*, 770–778.

Holdener, C.; and De Vlaminck, I. 2025. Smoothie: efficient inference of spatial co-expression networks from denoised spatial transcriptomics data. *bioRxiv*.

Hu, J.; Li, X.; Coleman, K.; Schroeder, A.; Ma, N.; Irwin, D. J.; Lee, E. B.; Shinohara, R. T.; and Li, M. 2021. SpaGCN: Integrating gene expression, spatial location and histology to identify spatial domains and spatially variable genes by graph convolutional network. *Nature Methods*, 18(11): 1342–1351.

Ji, A. L.; Rubin, A. J.; Thrane, K.; Jiang, S.; Reynolds, D. L.; Meyers, R. M.; Guo, M. G.; George, B. M.; Mollbrink, A.; Bergenstråhlé, J.; et al. 2020. Multimodal analysis of composition and spatial architecture in human squamous cell carcinoma. *Cell*, 182(2): 497–514.

Jøsang, A. 2016. *Subjective Logic*, volume 4. Springer.

Ju, W.; Fang, Z.; Gu, Y.; Liu, Z.; Long, Q.; Qiao, Z.; Qin, Y.; Shen, J.; Sun, F.; Xiao, Z.; et al. 2024a. A comprehensive survey on deep graph representation learning. *Neural Networks*, 106207.

Ju, W.; Gu, Y.; Chen, B.; Sun, G.; Qin, Y.; Liu, X.; Luo, X.; and Zhang, M. 2023. Glcc: A general framework for graph-level clustering. In *Proceedings of the AAAI Conference on Artificial Intelligence*, volume 37, 4391–4399.

Ju, W.; Yi, S.; Wang, Y.; Long, Q.; Luo, J.; Xiao, Z.; and Zhang, M. 2024b. A survey of data-efficient graph learning. In *International Joint Conference on Artificial Intelligence*, 8104–8113.

Ju, W.; Yi, S.; Wang, Y.; Xiao, Z.; Mao, Z.; Li, H.; Gu, Y.; Qin, Y.; Yin, N.; Wang, S.; Liu, X.; Yu, P. S.; and Zhang, M. 2025. A Survey of Graph Neural Networks in Real World: Imbalance, Noise, Privacy and OOD Challenges. *IEEE Transactions on Pattern Analysis and Machine Intelligence*, 1–20.

Kipf, T. N.; and Welling, M. 2017. Semi-supervised classification with graph convolutional networks. In *International Conference on Learning Representations*.

Levandowsky, M.; and Winter, D. 1971. Distance between sets. *Nature*, 234(5323): 34–35.

Li, H.; Song, J.; Gao, L.; Zhu, X.; and Shen, H. 2023. Prototype-based aleatoric uncertainty quantification for cross-modal retrieval. *Advances in Neural Information Processing Systems*, 36: 24564–24585.

Li, J.; Chen, S.; Pan, X.; Yuan, Y.; and Shen, H.-B. 2022. Cell clustering for spatial transcriptomics data with graph neural networks. *Nature Computational Science*, 2(6): 399–408.

Likas, A.; Vlassis, N.; and Verbeek, J. J. 2003. The global k-means clustering algorithm. *Pattern Recognition*, 36(2): 451–461.

Liu, T.; Fang, Z.-Y.; Li, X.; Zhang, L.-N.; Cao, D.-S.; and Yin, M.-Z. 2023. Graph deep learning enabled spatial domains identification for spatial transcriptomics. *Briefings in Bioinformatics*, 24(3): bbad146.

Long, Y.; Ang, K. S.; Li, M.; Chong, K. L. K.; Sethi, R.; Zhong, C.; Xu, H.; Ong, Z.; Sachaphibulkij, K.; Chen, A.; et al. 2023. Spatially informed clustering, integration, and

deconvolution of spatial transcriptomics with GraphST. *Nature Communications*, 14(1): 1155.

Loshchilov, I.; and Hutter, F. 2017. Decoupled weight decay regularization. *arXiv preprint arXiv:1711.05101*.

Lubeck, E.; Coskun, A. F.; Zhiyentayev, T.; Ahmad, M.; and Cai, L. 2014. Single-cell *in situ* RNA profiling by sequential hybridization. *Nature Methods*, 11(4): 360–361.

Malinin, A.; and Gales, M. 2018. Predictive uncertainty estimation via prior networks. In *Proceedings of the 32nd International Conference on Neural Information Processing Systems*, 7047–7058.

Maynard, K. R.; Collado-Torres, L.; Weber, L. M.; Uyttingco, C.; Barry, B. K.; Williams, S. R.; Catallini, J. L.; Tran, M. N.; Besich, Z.; Tippanni, M.; et al. 2021. Transcriptome-scale spatial gene expression in the human dorsolateral prefrontal cortex. *Nature Neuroscience*, 24(3): 425–436.

Moffitt, J. R.; Bambah-Mukku, D.; Eichhorn, S. W.; Vaughn, E.; Shekhar, K.; Perez, J. D.; Rubinstein, N. D.; Hao, J.; Regev, A.; Dulac, C.; et al. 2018. Molecular, spatial, and functional single-cell profiling of the hypothalamic preoptic region. *Science*, 362(6416): eaau5324.

Moran, P. A. 1950. Notes on continuous stochastic phenomena. *Biometrika*, 37(1/2): 17–23.

Pfitzner, D.; Leibbrandt, R.; and Powers, D. 2009. Characterization and evaluation of similarity measures for pairs of clusterings. *Knowledge and Information Systems*, 19(3): 361–394.

Pham, D.; Tan, X.; Balderson, B.; Xu, J.; Grice, L. F.; Yoon, S.; Willis, E. F.; Tran, M.; Lam, P. Y.; Raghubar, A.; et al. 2023. Robust mapping of spatiotemporal trajectories and cell–cell interactions in healthy and diseased tissues. *Nature Communications*, 14(1): 7739.

Rao, A.; Barkley, D.; França, G. S.; and Yanai, I. 2021. Exploring tissue architecture using spatial transcriptomics. *Nature*, 596(7871): 211–220.

Rodrigues, S. G.; Stickels, R. R.; Goeva, A.; Martin, C. A.; Murray, E.; Vanderburg, C. R.; Welch, J.; Chen, L. M.; Chen, F.; and Macosko, E. Z. 2019. Slide-seq: A scalable technology for measuring genome-wide expression at high spatial resolution. *Science*, 363(6434): 1463–1467.

Shah, S.; Lubeck, E.; Zhou, W.; and Cai, L. 2016. *In situ* transcription profiling of single cells reveals spatial organization of cells in the mouse hippocampus. *Neuron*, 92(2): 342–357.

Su, J.; Reynier, J.-B.; Fu, X.; Zhong, G.; Jiang, J.; Escalante, R. S.; Wang, Y.; Aparicio, L.; Izar, B.; Knowles, D. A.; et al. 2023. Smoother: a unified and modular framework for incorporating structural dependency in spatial omics data. *Genome Biology*, 24(1): 291.

Tang, Z.; Li, Z.; Hou, T.; Zhang, T.; Yang, B.; Su, J.; and Song, Q. 2023. SiGra: single-cell spatial elucidation through an image-augmented graph transformer. *Nature Communications*, 14(1): 5618.

Tu, W.; Zhou, S.; Liu, X.; Guo, X.; Cai, Z.; Zhu, E.; and Cheng, J. 2021. Deep Fusion Clustering Network. In *Proceedings of the AAAI Conference on Artificial Intelligence*, volume 35, 9978–9987.

Vaswani, A.; Shazeer, N.; Parmar, N.; Uszkoreit, J.; Jones, L.; Gomez, A. N.; Kaiser, L.; and Polosukhin, I. 2017. Attention is all you need. In *Proceedings of the 31st International Conference on Neural Information Processing Systems*, 6000–6010.

Veličković, P.; Cucurull, G.; Casanova, A.; Romero, A.; Lio, P.; and Bengio, Y. 2018. Graph attention networks. In *International Conference on Learning Representations*.

Vinh, N. X.; Epps, J.; and Bailey, J. 2009. Information theoretic measures for clusterings comparison: is a correction for chance necessary? In *Proceedings of the 26th International Conference on Machine Learning*, 1073–1080.

Wang, Y.; Song, B.; Wang, S.; Chen, M.; Xie, Y.; Xiao, G.; Wang, L.; and Wang, T. 2022. Sprod for de-noising spatially resolved transcriptomics data based on position and image information. *Nature Methods*, 19(8): 950–958.

Williams, C. G.; Lee, H. J.; Asatsuma, T.; Vento-Tormo, R.; and Haque, A. 2022. An introduction to spatial transcriptomics for biomedical research. *Genome Medicine*, 14(1): 68.

Wolf, F. A.; Angerer, P.; and Theis, F. J. 2018. SCANPY: large-scale single-cell gene expression data analysis. *Genome Biology*, 19: 1–5.

Xu, C.; Jin, X.; Wei, S.; Wang, P.; Luo, M.; Xu, Z.; Yang, W.; Cai, Y.; Xiao, L.; Lin, X.; et al. 2022. DeepST: identifying spatial domains in spatial transcriptomics by deep learning. *Nucleic Acids Research*, 50(22): e131–e131.

Yu, Z.; Lu, Y.; Wang, Y.; Tang, F.; Wong, K.-C.; and Li, X. 2022. ZINB-based graph embedding autoencoder for single-cell rna-seq interpretations. In *Proceedings of the AAAI Conference on Artificial Intelligence*, volume 36, 4671–4679.

Zhang, D.; Yu, N.; Yuan, Z.; Li, W.; Sun, X.; Zou, Q.; Li, X.; Liu, Z.; Zhang, W.; and Gao, R. 2024. stMMR: accurate and robust spatial domain identification from spatially resolved transcriptomics with multimodal feature representation. *GigaScience*, 13: giae089.

Zhu, J.; Li, Y.; Tang, Z.; and Chang, C. 2025. DUSTED: Dual-Attention Enhanced Spatial Transcriptomics Denoiser. In *Proceedings of the AAAI Conference on Artificial Intelligence*, volume 39, 1219–1227.

Zhu, Y.; He, X.; Tang, C.; Liu, X.; Liu, Y.; and He, K. 2024. Multi-view Adaptive Fusion Network for Spatially Resolved Transcriptomics Data Clustering. *IEEE Transactions on Knowledge and Data Engineering*.

## Appendix: Supplementary of Evidence-aware Integration and Domain Identification of Spatial Transcriptomics Data

### Pseudo-Code of PREST

Our proposed PREST can be summarized in Algorithm 1.

#### Algorithm 1: The Optimization Framework of PREST

**Input:** Spatial positions  $\mathbf{P} = \{(u_i, v_i)\}_{i=1}^N$ ; Gene expression matrix  $\mathbf{X} \in \mathbb{R}^{N \times G}$ ; Domain number  $K$ ; Maximum number of iterations  $I_{\max}$ ;

**Output:** Domain identification result  $\{y_1, \dots, y_N\}$ ;

- 1: Construct the spatial graph with adjacency matrix  $\mathbf{A}$ .
- 2: Initialize the model parameters and class prototypes;
- 3: **while** not converge **do**
- 4:   Update the spatial- and expression-level representations  $\mathbf{H}^s, \mathbf{H}^e$  through Eqs. (1)-(2);
- 5:   Perform structure-guided cross-attention mechanism to achieve fused representations  $\mathbf{H}$  in Eq. (3);
- 6:   Calculate spot-to-prototype and spot-to-spot similarity matrices  $\mathbf{E}, \mathbf{S}$  in Eq. (5);
- 7:   Estimate the belief and uncertainty of identification decision in Eq. (4);
- 8:   Compute the joint diversity-semantics learning loss  $\mathcal{L}_{DSL}$  in Eq. (6);
- 9:   Compute uncertainty-weighted ZINB-based reconstruction loss in  $\mathcal{L}_{UZR}$  in Eq. (7);
- 10:   Compute uncertainty-weighted spatial regularization loss  $\mathcal{L}_{USR}$  in Eq. (8);
- 11:   Perform backpropagation and update the entire network by minimizing  $\mathcal{L}$  in Eq. (9);
- 12: **end while**
- 13: Domain identification is performed by  $y_i = \arg \max_k \{b_{i1}, \dots, b_{iK}\}$  for all spots.

### Related Work

**GNN for Spatial Transcriptomics Data.** Spatial transcriptomics (ST) provides valuable information for studying the spatial distribution and functions of cells in tissues (Rao et al. 2021; Asp, Bergensträhle, and Lundeberg 2020). In recent years, Graph Neural Networks (GNNs) (Kipf and Welling 2017; Ju et al. 2023, 2024a) have shown great potential in processing such data (Liu et al. 2023; Li et al. 2022; Dong and Zhang 2022; Zhu et al. 2024). By modeling spatial relationships between cells as graph structures, GNNs can capture spatial dependencies among cells, thereby enhancing the understanding of spatial patterns in gene expression. For example, GNNs have been used to analyze spatial transcriptomics data from mouse brains, revealing gene expression differences and spatial patterns across brain regions (Hu et al. 2021). Additionally, GNNs have been utilized for tasks such as spatial domain identification, cell type annotation, and trajectory inference (Xu et al. 2022; Long et al. 2023; Zhang et al. 2024; Zhu et al. 2025). However, current GNNs fail to capture the belief and uncertainty in decision-making

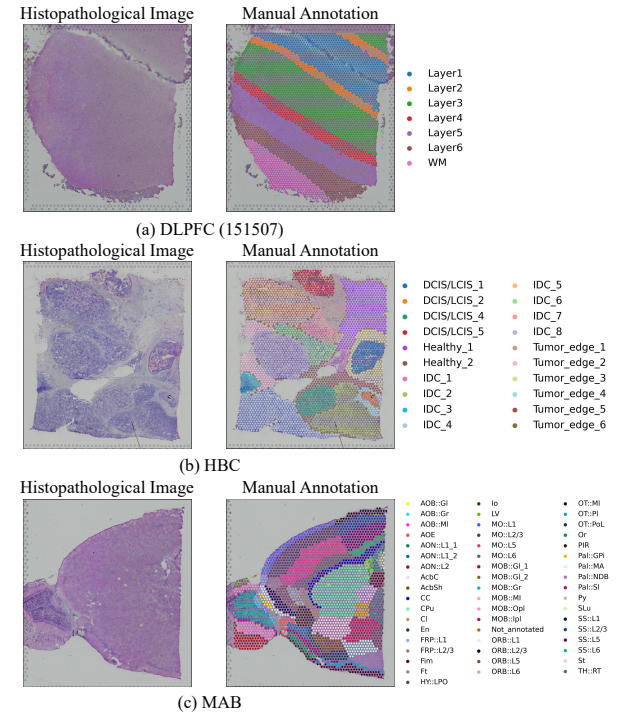


Figure 6: Data images and manual annotations.

caused by noise in spatial transcriptomics data. Our proposed PREST, which incorporates evidence and belief, addresses this limitation by effectively handling points of varying quality in a fine-grained manner, thereby enhancing the accuracy of downstream tasks.

**Denoising of Spatial Transcriptomics Data.** ST data are frequently affected by sequencing errors, background signals, and sample preparation biases, lowering data quality and downstream analyses (Du et al. 2024). Recent efforts have increasingly leveraged spatial information to enhance denoising. For instance, Sprod (Wang et al. 2022) integrates spatial coordinates and histological images via latent graph learning for efficient denoising and imputation. Similarly, STAGATE (Dong and Zhang 2022) uses graph attention to model heterogeneous local expression patterns, improving spatial domain detection. Building on this direction, Smoother (Su et al. 2023) incorporates modular spatial priors to support expression recovery and cell-type deconvolution, even in non-spatial models. More recently, SiGra (Tang et al. 2023) applies hybrid graph transformers over cell-level graphs and multi-channel histology to enhance expression inference in noisy, low-expression data. In contrast, our PREST leverages class prototypes and subjective logic to model belief and uncertainty from noisy or dropout ST data, enabling uncertainty-aware reconstruction that down-weights unreliable spots and improves robustness.

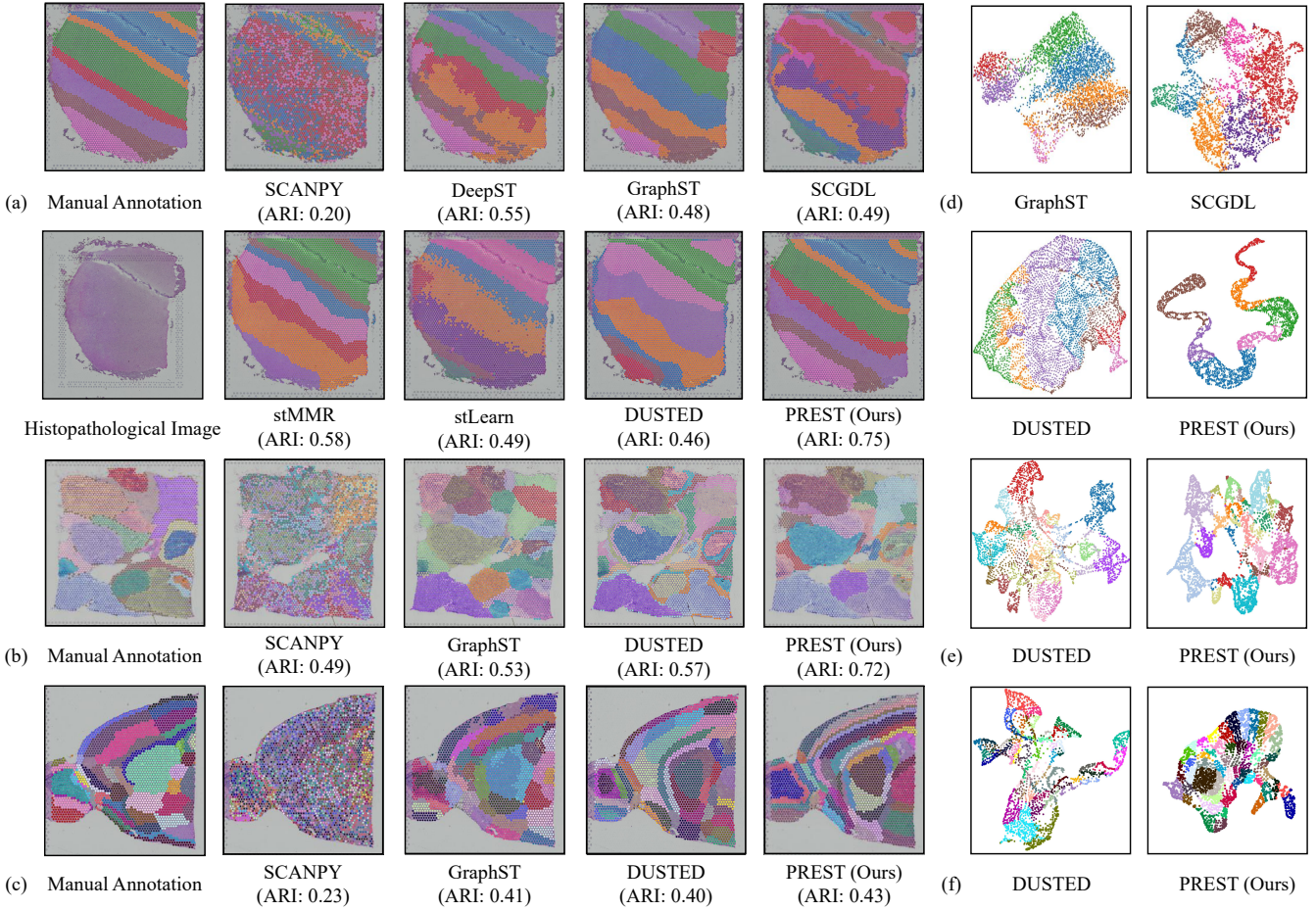


Figure 7: Visualization of domain identification of different methods on (a),(d) DLPFC (151507) (b),(e) HBC (c),(f) MAB datasets. The **bold** and underlined values indicate the best and the runner-up results, respectively

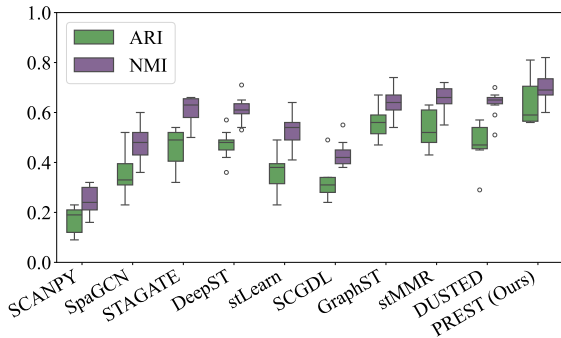


Figure 8: The box plot of the ARI and NMI values of our PREST on DLPFC.

## Additional Experimental Results

### Complete Visualization of Domain Identification

To further validate the effectiveness of our method PREST, we present domain identification visualization and UMAP visualization, as shown in Figure 7, which displays com-

parative domain identification results and UMAP visualizations for various methods across three spatial transcriptomics datasets: DLPFC (151507), HBC, and MAB. It can be observed that our PREST consistently demonstrates superior identification quality, achieving well-defined domain boundaries and high concordance with expert annotations in all cases. In contrast, non-spatial methods such as SCANPY fail to capture spatial autocorrelation within biological domains due to their omission of spatial context, resulting in fragmented and inconsistent domain assignments. This limitation is further evidenced in UMAP visualizations, where our proposed PREST exhibits tightly clustered domains with distinct hierarchical organization, while competing approaches display significant inter-domain overlap. Such differences highlight the superior spatial coherence and structural fidelity of our results, underscoring PREST's effectiveness in preserving spatial information.

### Box plot of ARIs and NMIs on DLPFC

To facilitate comparative analysis of domain identification performance across different methods, we present boxplot visualizations of results across all DLPFC slices, as shown

Dataset	Metric	SCANPY	stLearn	SCGDL	GraphST	stMMR	DUSTED	PREST (Ours)
HBC	ARI	0.49	0.55	0.35	0.53	<b>0.62</b>	0.57	<b>0.72</b>
	NMI	0.52	0.63	0.43	<u>0.67</u>	<u>0.67</u>	0.65	<b>0.73</b>
MAB	ARI	0.23	0.38	0.26	<u>0.41</u>	0.40	0.40	<b>0.43</b>
	NMI	0.45	0.66	0.64	<u>0.71</u>	0.68	0.70	<b>0.72</b>

Table 5: Domain identification performance on HBC and MAB datasets. The **bold** and underlined values indicate the best and the runner-up results, respectively.

Model	Metric	SCANPY	STAGATE	GraphST	DUSTED	PREST (Ours)
DLPFC (151507)	Jaccard	0.31	<b>0.49</b>	0.37	0.40	<b>0.65</b>
	Moran's I	0.47	<u>0.86</u>	0.77	0.66	<b>0.90</b>
HBC	Jaccard	0.22	0.31	0.40	<u>0.43</u>	<b>0.47</b>
	Moran's I	0.36	<u>0.77</u>	0.76	0.62	<b>0.79</b>
MAB	Jaccard	0.15	<u>0.25</u>	0.23	0.22	<b>0.28</b>
	Moran's I	0.17	<u>0.74</u>	0.59	0.64	<b>0.82</b>

Table 6: Performance comparison of Jaccard similarity coefficient and Moran's I score across three datasets. The **bold** and underlined values indicate the best and the runner-up results, respectively.

in Figure 8. Critically, our PREST achieves median scores of 0.64 (ARI) and 0.70 (NMI), with tight interquartile ranges indicating consistent performance. These results represent absolute improvements of +0.08 in ARI and +0.05 in NMI over the second-best performing methods, confirming superior robustness in spatial domain identification.

### Comparison of ARI and NMI on HBC and MAB

To rigorously assess and compare domain identification performance across other benchmark datasets, we evaluate our method against other baselines on HBC and MAB, as summarized in Table 5. From the results, we observe that PREST consistently achieves state-of-the-art results on both HBC dataset and MAB dataset, notably attaining absolute improvements of 0.10 in ARI and 0.06 in NMI over the second-best method (stMMR) on HBC. These quantitative advances directly correspond to PREST's enhanced ability to resolve biologically meaningful spatial domains, as evidenced by histologically consistent domain boundaries.

### Comparison under Other Metrics

To rigorously evaluate spatial domain coherence, we benchmark PREST against established methods using Jaccard similarity (quantifying the concordance between domain identification results and ground truth) and Moran's I (measuring spatial autocorrelation of domain assignments) across three benchmark datasets, as shown in Table 6. Building on this framework, PREST achieves statistically significant improvements over all baselines, with +0.16 higher Jaccard score on DLPFC slice 151507 and superior spatial autocorrelation (Moran's I = 0.79 vs. STAGATE's 0.77) on HBC. Critically, non-spatial methods like Scanpy exhibit severe degradation in spatial coherence, demonstrating that explicit spatial modeling is fundamentally necessary for biologically

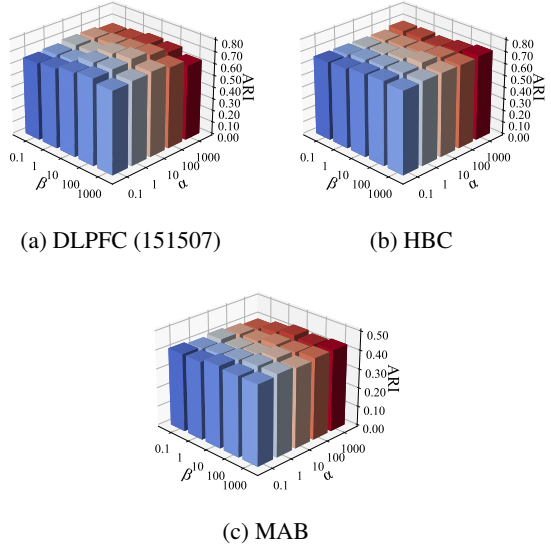


Figure 9: Sensitivity analysis of loss weights  $\alpha$  and  $\beta$ .

meaningful domain identification.

### Hyperparameter Sensitivity Analysis

To assess robustness to hyperparameter variations across all datasets, we perform comprehensive sensitivity analysis of loss weights  $\alpha$  and  $\beta$ , as shown in Figure 9. The analysis reveals PREST's consistent performance stability across parameter ranges, with particularly robust domain identification observed for  $\alpha \in [1, 100]$  and  $\beta \in [10, 100]$  where ARI and NMI metrics remain consistently high. Critically, the stability enables reliable spatial domain identification without parameter tuning, demonstrating PREST's practical robustness in biological applications.

### Performance Comparison on DLPFC (151507) and HBC under Different Noise

To evaluate PREST's robustness under realistic noise conditions, we conduct perturbation HBC and DLPFC tissue slice 151507, as presented in Table 7. This analysis reveals PREST's consistent domain identification performance across Gaussian noise (variances 1 and 5) and dropout noise (probabilities 0.3 and 0.6), achieving ARIs of 0.48/0.36 under Gaussian noise and 0.57/0.51 under dropout noise on HBC. Critically, this stability may stem from our method's capability of modeling spot uncertainty, which helps avoid low-quality overfitting while effectively learning robust spot representations. Furthermore, as quantitatively demonstrated in Table 7, where dropout-induced degradation remains substantially lower than Gaussian-induced degradation across all methods, this consistent pattern confirms that spatial transcriptomic frameworks inherently align with biologically meaningful sparsity patterns, where dropout effects mirror natural data characteristics.

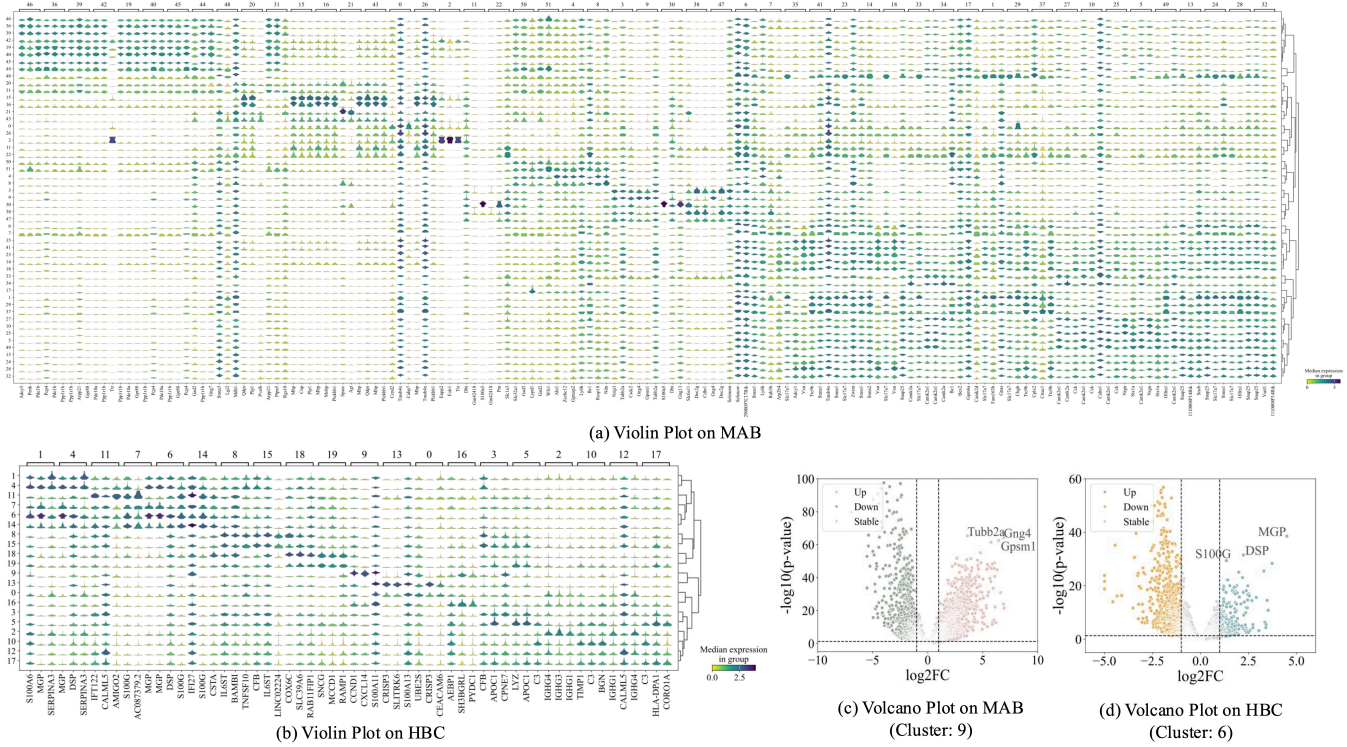


Figure 10: DEG detection on the MAB and HBC datasets.

## Additional Downstream Analysis

### Detection of HBC and MAB

To evaluate biological relevance, we perform differential expression analysis using PREST’s spatially domains. This analysis reveals PREST’s superior sensitivity in detecting biologically meaningful DEGs, as demonstrated by the violin plots in Figure 10(a)-10(b). Critically, this enhanced resolution captures nuanced biological mechanisms, exemplified by MGP in HBC (Gong et al. 2019): its significant upregulation in triple-negative breast cancer promotes proliferation and metastasis, while downregulation in ER-positive subtypes correlates with chemoresistance and poorer outcomes—patterns only detectable through PREST’s precise domain delineation. Consistent with this biological resolution, the volcano plots in Figure 10(c)-10(d) further confirm PREST’s effectiveness in preserving interpretable transcriptomic signatures across HBC and MAB datasets, establishing its capability for spatially informed biological discovery.

### Expression Imputation on Genes PLP1 of DLPFC and Efhd2 of MAB

To further validate biological relevance, we extend imputation experiments to marker genes across benchmark datasets. Figure 11 quantitatively demonstrates PREST’s superior performance in imputing PLP1 for DLPFC and Efhd2 for MAB, where the method precisely reconstructs quantitative expression values while maintaining biological relevance across spatial domains. Critically, this molecular fi-

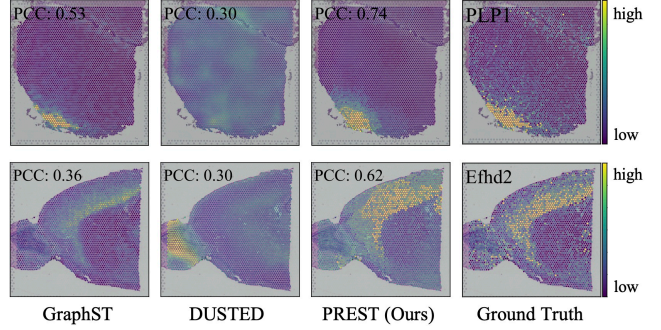


Figure 11: Visual comparison of gene expression imputation (PLP1 and Efhd2) for DLPFC and MAB, respectively.

delity enables the preservation of distinctive spatial distribution patterns, as evidenced by substantial PCC improvements of +0.21 for PLP1 and +0.26 for Efhd2 over baselines. Consequently, these results establish that PREST not only recovers missing gene expression values with high accuracy but also maintains the critical spatial context essential for biological interpretation in spatial transcriptomics.

### Pathway Enrichment Analysis.

To validate PREST’s biological utility, we perform KEGG pathway analysis on Layer 6 of DLPFC slice 151507, mapping differentially expressed genes to functional patchway to elucidate regulatory mechanisms in cortical orga-

Method	Raw	Gaussian Noise		Dropout	
		$\epsilon = 1$	$\epsilon = 5$	$p = 0.3$	$p = 0.6$
GraphST	0.48	0.21	0.10	0.40	0.17
DUSTED	0.46	0.19	0.12	0.37	0.16
PREST (Ours)	<b>0.75</b>	<b>0.49</b>	<b>0.34</b>	<b>0.60</b>	<b>0.55</b>

(a) DLPFC (151507)

Method	Raw	Gaussian Noise		Dropout	
		$\epsilon = 1$	$\epsilon = 5$	$p = 0.3$	$p = 0.6$
GraphST	0.53	0.23	0.14	0.36	0.34
DUSTED	0.57	0.31	0.19	0.39	0.34
PREST (Ours)	<b>0.72</b>	<b>0.48</b>	<b>0.36</b>	<b>0.57</b>	<b>0.51</b>

(b) HBC

Table 7: Performance comparison under Gaussian noise and dropout noise on (a) DLPFC (151507) and (b) HBC via ARI ( $\epsilon$ : variance of Gaussian noise,  $p$ : dropout probability).

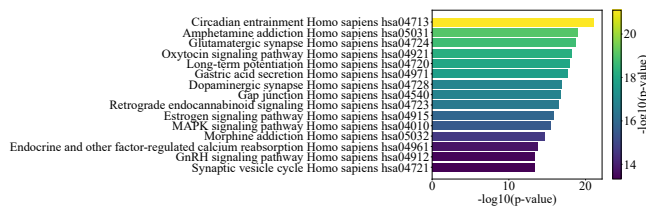


Figure 12: KEGG pathway enrichment visualization.

nization. As quantified in Figure 12, PREST reveals significant enrichment in the circadian entrainment pathway (hsa04713), wherein phototransduction cascades synchronize the suprachiasmatic nucleus (SCN) master clock via environmental light cues. This finding strongly correlates with the established biological function of Layer 6, namely, its critical role in regulating sleep rhythms and attention, which confirms PREST’s superior capability in resolving complex, spatially-contextualized regulatory mechanisms.

## Complete Experimental Setup

**Datasets.** To validate the superiority of our PREST, we conduct extensive experiments on three benchmark datasets related to spatial transcriptomics. The first dataset is derived from the LIBD study of the human dorsolateral prefrontal cortex (DLPFC), which consists of multiple tissue slices and includes expert-curated annotations by Maynard et al. (2021). The second dataset comes from the 10x platform, which contains human breast cancer (HBC) samples (Buache et al. 2011). The third dataset is the mouse anterior brain (MAB) tissue, which is annotated with 52 different regions and contains 32,285 genes (Dong 2008). The image and manual annotations are presented in Figure 6.

**Baselines.** We compare our PREST with several state-of-the-art models, including classical non-spatial clustering methods, i.e., SCANPY (Wolf, Angerer, and Theis 2018),

and spatial clustering methods, i.e., SpaGCN (Hu et al. 2021), STAGATE (Dong and Zhang 2022), DeepST (Xu et al. 2022), stLearn (Pham et al. 2023), SCGDL (Liu et al. 2023), GraphST (Long et al. 2023), stMMR (Zhang et al. 2024), and DUSTED (Zhu et al. 2025).

**Evaluation Metrics.** To evaluate the domain identification performance, we adopt the supervised Adjusted Rand Index (ARI, Vinh, Epps, and Bailey 2009), Normalized Mutual Information (NMI, Pfitzner, Leibbrandt, and Powers 2009) and the Jaccard similarity coefficient (Levandowsky and Winter 1971) as performance evaluation metrics, which are used to assess the quality of clustering results and the consistency between predicted clustering labels and the ground truth cluster labels, respectively. For unsupervised assessment, we further compute Moran’s I (Moran 1950) to quantify spatial autocorrelation of cluster assignments. For each metric, a larger value indicates better performance.

**Implement Details.** For all datasets, we first filter out genes with extremely low expression or variance, then select the top 3,000 genes with the highest variance. Based on this, we construct an undirected spatial graph using Euclidean distance with a fixed radius  $r$  (set to 550 in our experiments) to capture spatial relationships. We adopt a pre-training procedure similar to DFCN (Tu et al. 2021), with key modifications including adjusted network depth, fusion strategy, training epochs, and the integration of self-attention and skip connections. The PREST model is implemented in PyTorch v2.4 platform and trained on a single NVIDIA RTX 3090 GPU with 24GB of memory. We use the AdamW (Loshchilov and Hutter 2017) optimizer with a learning rate of 1e-3 for the DLPFC dataset and 1e-4 for the others. Based on hyperparameter tuning,  $\alpha$  and  $\beta$  are consistently fixed at 10 and 100, respectively, across all datasets.